

Lattice Boltzmann Models of Charged Multiphase Flows for Electrospinning Simulations

Marco Lauricella,^{1,*} Simone Melchionna,² Andrea Montessori,³
Dario Pisignano,^{4,5} Giuseppe Pontrelli,¹ and Sauro Succi^{1,6}

¹*Istituto per le Applicazioni del Calcolo CNR,
Via dei Taurini 19, 00185 Rome, Italy*

²*Istituto dei Sistemi Complessi CNR,
Consiglio Nazionale delle Ricerche, Dipartimento di Fisica,
Università di Roma Sapienza, P.le A. Moro 2, 00185 Rome, Italy*

³*Department of Engineering, University of Rome "Roma Tre,
" Via della Vasca Navale 79, 00141 Rome, Italy*

⁴*Dipartimento di Fisica, Università di Pisa,
Largo B. Pontecorvo 3, 56127 Pisa, Italy*

⁵*NEST, Istituto Nanoscienze-CNR, Piazza S. Silvestro 12, 56127 Pisa, Italy*

⁶*Harvard Institute for Applied Computational Science,
Cambridge, Massachusetts, United States*

Abstract

We present a Shan-Chen model for charged leaky dielectric multiphase fluids in the context of electrospinning simulations. The role of non-linear rheology on the dynamics of electrified jets is considered by exploiting the Carreau model for pseudoplastic fluids. We report exploratory simulations of charged droplets at rest and under a constant electric field, and we provide results for charged jet formation under electrospinning-like conditions.

* Corresponding author: m.lauricella@iac.cnr.it

I. INTRODUCTION

The dynamics of charged jets presents a major interest, both as an outstanding problem in non-equilibrium thermodynamics, as well as for its numerous applications in science and engineering [1–3]. In particular, the recent years have witnessed a surge of interest towards the manufacturing of electrospun nanofibers, mostly on account of their prospective applications, such as tissue engineering, air and water filtration, optoelectronics, drug delivery and regenerative medicine [3–5]. As a consequence, several experimental studies have focused on the characterization and production of one-dimensional elongated nanostructures [5–9]. Electrospun nanofibers are typically produced at laboratory scale via the uniaxial stretching of a jet, which is ejected at a nozzle from an electrified charged polymer solution. The charged jet elongates under the effect of an external electrostatic field applied between the spinneret and a conductive collector and eventually undergoes electromechanical (e.g., whipping) instabilities due to various sources of disturbance, such as mechanical vibrations at the spinneret, hydrodynamic friction with the surrounding fluid and others [10]. While such instabilities can be detrimental in some respect, making an accurate position of individual fibers on target substrates very hard, in other experiments they are sought for, since they result in thinner cross sections, hence finer electrospun fibres, as they hit the collector [4]. This follows from a plain argument of mass conservation: whipping instabilities generate longer jets, hence thinner cross sections [11].

The computational modelling of the electrospinning process is based on two main families of techniques: particle methods and Lagrangian fluid methods. The former is based on the representation of the polymer jet as a discrete collection of discrete particles (beads) connected via elastic springs with frictional coupling (dissipative dashpots) and interacting via long-range Coulomb electrostatics [10, 12–14]. The latter, on the other hand, describe the jet as a continuum media, obeying the Navier-Stokes equations for a charged fluid in Lagrangian form [15–17]. Both methods are grid-free, hence well suited to describe abrupt changes of the jet morphology without taxing the grid resolution, as it is the case for Eulerian grid methods.

In this respect, grid-based methods, such as Lattice Boltzmann (LB), are not expected to offer a competitive alternative to the two aforementioned class of methods. Nevertheless, owing to its efficiency, especially on parallel computers, and its flexibility towards the in-

clusion of physical effects beyond single-phase hydrodynamics, it appears worth exploring the possibility of using LB also in the framework of electrified fluids and jets. For instance, in the last decade significant improvements in LB methods for modelling microfluidic flows containing electrostatic interactions have been achieved [18, 19], opening new applications of LB methods in electrohydrodynamic problems [20–24]. In particular, LB methods were successfully employed to simulate deformations and breakup of conductive vapor bubbles, bubble deformation due to electrostriction, dynamics of drops with different electric permittivity. All these investigations usually exploit the approach originally introduced by A. L. Kupershtokh and D. A. Medvedev [19], where dielectric liquids are assumed with zero free charge density, so that the charge carriers are essentially locally bounded to the material [25]. Within this assumption, charge carriers are explicitly modeled by a convective transport equation solved by a second LB solver, taking into account the rates of ionization and recombination of charge carriers fluctuating around a local value (distribution) of equilibrium.

In the 1960s, G. I. Taylor provided several considerations for dealing with electrified fluid in a series of papers [26–28]. In particular, Taylor discovered that a moving charged fluids cannot be considered either as a perfect dielectric or as a perfect conductor. Instead, the fluid acts as a "leaky dielectric liquid", where a non-zero free charge is mainly accumulated on the interface between the charged liquid and the gaseous phase [29]. As a consequence, the charge produces electric stresses different from those observed in perfect conductors or perfect dielectrics. Indeed, in the last cases the charge induces a stress which is perpendicular to the interface, altering the interface shape to balance the extra stress. In the electrospinning process, the non-zero electrostatic field tangent to the liquid interface produces a non-zero tangential stress on the interface which is balanced from the viscous force [16].

The present work introduces a LB method for simulating charged leaky dielectric liquids, which is of main interest for modeling the electrospinning process. In this context, the largest part of the charge is modeled to lie along the interface between the liquid and the gaseous phase in similarity with previous works [30, 31]. Further, the present LB approach is generalized to the case of non-Newtonian flows with shear-thinning viscosity in order to account the rheological properties of electrospun jets. In this context, we adopt an entropic approach [32, 33] in order to preserve locally the second principle (H- theorem) also in presence of sharp changes in the fluid viscosity and structure.

The paper is organised as follows. In section II we present the basic features of the LB extension to the case of charged multiphase fluids. In sections III, we present results for the case of charged multiphase fluids at rest, and we report on preliminary results for charged multiphase jets under conditions related to electrospinning experiments.

II. MODEL

We consider a single species, charged fluid as composed of point-like particles and neglect correlations stemming from excluded volume interactions. Following Boltzmann's description, the state of the fluid is determined by the distribution function $f_p(\vec{r}, t)$ being the probability of finding at time t the fluid at position \vec{r} and moving with discrete velocity \vec{c}_p , with $p = 1, b$ given b the number of lattice directions. Here, the velocities \vec{c}_p are also viewed as vectors connecting a lattice site \vec{r} to its lattice neighbors. The LB equation reads

$$f_p(\vec{r} + \vec{c}_p \Delta t, t + \delta t) = f_p(\vec{r}, t) - \alpha\beta(f_p - f_p^{eq}(\rho, \vec{u})) + S_p(\vec{r}, t), \quad (1)$$

where the product $\alpha\beta$ plays the role of a collision frequency, S_p is a source term (see below), and f_p^{eq} is the continuum Maxwell-Boltzmann distribution computed at density ρ and velocity \vec{u} [32]. The macroscopic variables are given by the density $\rho = \sum_p f_p$ and the fluid velocity $\vec{u} = 1/\rho \sum_p \vec{c}_p f_p$. In the following, we refer to lattice units where the mesh spacing and timestep Δt are conveniently set to unity. Also, we adopt the so-called D2Q9 scheme, composed by 8 discrete speeds (connecting first and second lattice neighbors) and one extra null vectors accounting for particles at rest. In this scheme, Here, the f_p^{eq} are chosen as a second-order Mach-number expansion

$$f_p^{eq} = w_p \rho \left[1 + \frac{\vec{u} \cdot \vec{c}_p}{c_s^2} + \frac{(\vec{u} \cdot \vec{c}_p)^2 - c_s^2 u^2}{2c_s^4} \right] \quad (2)$$

where the w_p are weights equal to 4/9 for the rest particles, 1/9 and 1/36 respectively for the smallest and largest velocities \vec{c}_p , and c_s is the speed of sound that in lattice units is equal to $1/\sqrt{3}$. At the same time, we consider a unit fluid molecular mass, so that the thermal energy is equal to $k_B T = c_s^2$ with k_B the Boltzmann constant and T the temperature. Following the approach of Refs. [32–34], the factor β in Eq. 1 depends on the kinematic viscosity ν by the relation

$$\beta = \frac{2c_s^2}{2\nu + c_s^2}, \quad (3)$$

while α is the largest value of the over-relaxation parameter so that the local entropy reduction can be avoided, ensuring the H- theorem. In particular, α is computed as the root of the scalar nonlinear equation [33, 35]

$$H(f + \alpha(f^{eq} - f)) = H(f), \quad (4)$$

where H denotes the Boltzmann's entropy function, defined in discrete form [36] as

$$H(f) \equiv \sum_p f_p \ln \left(\frac{f_p}{w_p} \right). \quad (5)$$

In Eq. 1, the source term S_p takes into account the global effect of all the internal and external forces \vec{F} . This is assessed by the exact difference method proposed by Kupershtokh et al. [37], which reads

$$S_p = f_p^{eq}(\rho, \vec{u} + \Delta\vec{u}) - f_p^{eq}(\rho, \vec{u}), \quad (6)$$

where $\Delta\vec{u} = \vec{F}/\rho$. In bulk conditions, the LB method is intrinsically second-order accurate in space and time, and, in order to ensure the same accuracy in presence of forces, the local velocity is taken at half time step

$$\rho\vec{u} = \sum_p f_p(\vec{r}, t)\vec{c}_p + \frac{1}{2}\vec{F}. \quad (7)$$

Here, the total body force $\vec{F} = \vec{F}_{int} + \vec{F}_{el}$ includes the inter-particle force \vec{F}_{int} and the electric force \vec{F}_{el} . The electric force acting on the boundary point \vec{r} between a gas and a fluid with the local non-uniform permittivity $\varepsilon(\vec{r})$ in an electric field \vec{E} reads [25, 29]

$$\begin{aligned} \vec{F}_{el} &= q\vec{E} - \frac{1}{2}|E|^2\nabla\varepsilon + \frac{1}{2}\nabla\left(|E|^2\rho\frac{\partial\varepsilon}{\partial\rho}\right) \\ &= q\vec{E} + \frac{1}{2}\rho\frac{\partial\varepsilon}{\partial\rho}\nabla|E|^2, \end{aligned} \quad (8)$$

where q is the local free charge carried on the fluid. In the last Eq., the vacuum permittivity ε_0 was assumed equal to 1 as in the Gaussian centimetre-gram-second (cgs) unit system, so that the charge in lattice units is $length^{3/2} mass^{1/2} time^{-1}$ in similarity with the statcoulomb definition (note that Coulomb's constant is also 1). For the sake of convenience, we report in Appendix the units conversion Table in cgs dimensions from lattice units for several physical quantities shown in the following. As in Ref. [19], we consider a fluid with permittivity $\varepsilon = 1 + \rho/\rho_0$ with ρ_0 an arbitrary constant (in the following taken for simplicity equal to 1) so that it is $\rho(\partial\varepsilon/\partial\rho) = \varepsilon - 1$. As a consequence, Eq. 8 reduces to

$$\vec{F}_{el} = q\vec{E} + \frac{\varepsilon - 1}{2}\nabla|E|^2. \quad (9)$$

In the following, we assume that the magnetic induction effects can be neglected so $\nabla \times \vec{E} = 0$, and the system follows the Gauss law $\nabla \cdot (\varepsilon \vec{E}) = q$. Since $\vec{E} = -\nabla \phi$ with ϕ the electric potential, the Poisson equation $div(\varepsilon(\vec{r})\nabla\phi) = -q(\vec{r})$ can be solved at each lattice node \vec{r} , given the boundary conditions of the system and the local charge $q(\vec{r})$ at the node (specified below). In particular, we determine the electric potential by solving numerically the two-dimensional Poisson equation by means of a SOR (Successive Over-Relaxation) algorithm and the Gauss-Seidel method [38]. Note that the Poisson equation includes the non-uniformity of the permittivity $\varepsilon(\vec{r})$, and it is solved on-the-fly during the simulation. Hence, the electric force $\vec{F}_{el} = q(-\nabla\phi)$ is added into the LB scheme by Eq. 6.

Since we are modeling a leaky dielectric fluid, we assume that the free charge in the system is mainly distributed over the liquid-gaseous interface. Further, in similarity to previous electrospinning models [16, 17], the relaxation time of free charge in the system is assumed to be irrelevant. In other words, the free charge in bulk liquid relaxes to the liquid interface in a smaller time than any other characteristic time in the system [39]. This is a well-established assumption of a leaky dielectric fluid (for further details see Ref. [29]). The liquid charge in the point \vec{r} is given as

$$q = q_b + q_s, \quad (10)$$

which is the sum of a surface charge q_s and a small bulk term q_b . The bulk term q_b is taken as

$$q_b(\vec{r}) = Q_b \frac{\rho(\vec{r}) \theta(\rho(\vec{r}); \rho_0)}{\int \rho(\vec{r}) \theta(\rho(\vec{r}); \rho_0) d\vec{r}}, \quad (11)$$

where Q_b denotes the total charge in the bulk, the denominator acts to keep constant the charge due to the charge conservation principle, and $\theta(\rho; \rho_0)$ denotes a smoothed version of the Heaviside step function switching from zero to one at ρ_0 (equal to 1 in all the following simulations) in order to select only the liquid phase. The term q_s is modeled as a proportional to the absolute density gradient

$$q_s(\vec{r}) = Q_s \frac{|\nabla\rho(\vec{r})|^2}{\int |\nabla\rho(\vec{r})|^2 d\vec{r}}, \quad (12)$$

where Q_s denotes the total charge over the surface, and the denominator ensures the charge conservation principle as in the previous case. This approach is usually referred to as the constant surface charge model, and it was already adopted in Refs [30, 31] as a strategy to simplify the charge transport and distribution on the droplet interface. Nonetheless, the

constant surface charge model fails in describing a distributed charge on the drop interface whenever the charge density is high, since the curvature surface alters the local charge density [16]. In order to address the issue, we assume that the curvature biases the surface charge density as in a conductive liquid, following the power-law introduced by I. W. McAllister [40], which states

$$q_s = q_{s,max}(K/K_{max})^{\frac{1}{4}}. \quad (13)$$

Here, K denotes the mean curvature $K = \nabla \cdot \hat{n}$ with the local interface normal $\hat{n} = \nabla\rho(\vec{r})/|\nabla\rho(\vec{r})|$ [41], while $q_{s,max}$ is the maximum surface charge at the maximum curvature K_{max} chosen as a reference value for the system under investigation. It is worth to emphasize that treating a leaky dielectric as a conductive liquid is a simplification already made by several authors (e.g., G. Taylor [26], A. Yarin et al. [42], etc.). For the sake of simplicity, we take in the following the maximum curvature K_{max} equal to K_d value, defined as the curvature doubling the local surface charge density. Thus, we rewrite Eq. 10 as

$$q(\vec{r}) = Q_b \frac{\rho(\vec{r}) \theta(\rho(\vec{r}); \rho_0)}{\int \rho(\vec{r}) \theta(\rho(\vec{r}); \rho_0) d\vec{r}} + Q_s \frac{|\nabla\rho(\vec{r})|^2 [1 + (K/K_d)^{\frac{1}{4}}]}{\int |\nabla\rho(\vec{r})|^2 [1 + (K/K_d)^{\frac{1}{4}}] d\vec{r}}. \quad (14)$$

The total charge of the system is conserved and equal to $Q = Q_b + Q_s$.

In addition, the fluid is subjected to an internal thermodynamic force \vec{F}_{int} promoting a phase separation. The phase separation force is accounted for by means of the Shan-Chen method [43]. We construct the local force as

$$\vec{F}_{int}(\vec{r}, t) = - \left[G \sum_{p \in fluid} w_p \psi(\rho(\vec{r} + \vec{c}_p, t)) \vec{c}_p + G_w \sum_{p \in wall} w_p \psi(\rho(\vec{r}, t)) \vec{c}_p \right] \psi(\rho(\vec{r}, t)) \quad (15)$$

with the sum $\sum_{p \in fluid}$ running over lattice nodes where the fluid is allowed, that is, not belonging to the wall, and $\sum_{p \in wall}$ runs over nodes belonging to the wall. G and G_w are fluid-fluid and fluid-wall interaction strengths, respectively. In Eq 15, ψ is an effective number density, which is taken for simplicity $\psi(\rho) = \rho_0[1 - \exp(-\rho/\rho_0)]$, being ρ_0 an arbitrary constant [44] (in the following assumed equal to 1).

A. Extension to Non-Newtonian flows

In the electrospinning process, the rheological behavior of polymeric liquid with shear-rate-dependent viscosity is expected to play a significant role on jet dynamics. As a consequence, we now generalize the present model to the case of non-Newtonian flows, in similarity

with the approach reported in Refs [45–47]. The shear-rate $\dot{\gamma}$ is a functional of the density distribution function f . In particular, the strain tensor $\mathbf{\Gamma}_{\eta,\delta}$ reads [45, 48]

$$\mathbf{\Gamma}_{\eta,\delta} = -\frac{1}{2\rho\tau c_s^2}\mathbf{\Pi}_{\eta,\delta}, \quad (16)$$

where

$$\mathbf{\Pi}_{\eta,\delta} = \sum_p (f_p - f_p^{eq}) \vec{c}_{p\eta} \vec{c}_{p\delta}, \quad (17)$$

is the the stress tensor with η and δ running over the spatial dimensions. Note that τ in Eq. 16 is defined as the inverse of the product $\alpha\beta$, where α was computed by Eq. 4, and β depends by Eq. 3 on the kinematic viscosity ν . We now rewrite Eq. 16 as

$$\dot{\gamma} = \frac{\mathbf{\Pi}}{\rho\tau(\dot{\gamma})c_s^2}, \quad (18)$$

where $\dot{\gamma}$ and $\mathbf{\Pi}$ are computed as matrix 2-norm $\dot{\gamma} = 2\|\mathbf{\Gamma}\|_2$ and $\mathbf{\Pi} = \|\mathbf{\Pi}\|_2$ of the shear and stress tensor [45], respectively. Note that in the last Eq. we exploit a constitutive relation between the kinematic viscosity ν and the shear-rate $\dot{\gamma}$, so that $\tau = \tau(\dot{\gamma})$. As a consequence, $\dot{\gamma}$ is computed as the root of the scalar nonlinear Eq. 18.

We should now consider the general trend observed in electrospun polymeric filaments [49]. As main features, we highlight that a polymeric spinning solution at low shear rate behaves as a quasi-Newtonian fluid with viscosity ν_0 , since the initial condition can be recovered, while at high shear rate a non-reversible disentanglement is present. In particular, it is possible to identify a retardation time λ at which the shear-thinning starts, which is equal to the inverse value of the shear rate at that instant. At very high shear rate, a quasi-Newtonian behavior is again observed as soon as the alignment of the polymer chains is extremely high (almost complete). The last region is characterized by a final viscosity value (infinite viscosity ν_∞), which is lower than ν_0 .

In the present investigation, we exploit the Carreau model [50], which is able to describe all the mentioned rheological properties. The Carreau model states that

$$\nu(\dot{\gamma}) = \nu_\infty + (\nu_0 - \nu_\infty) \left[1 + (\lambda\dot{\gamma})^2\right]^{(n-1)/2}, \quad (19)$$

where n is the flow index ($n < 1$ for a pseudoplastic fluid). Obtained $\dot{\gamma}$ by resolving Eq. 18 and $\nu(\dot{\gamma})$ by Eq. 19, and assuming a slow variation of $\nu(\dot{\gamma})$ over the time Δt , the local parameter β is finally estimated by Eq. 3. Note that a validation of a similar implementation in LB scheme of the Carreau model was given in Ref. [45].

III. NUMERICAL RESULTS

A. Charged drop

In order to assess the properties of our implementation for charged multiphase systems, we have initially run a set of simulations modeling a charged leaky dielectric fluid system obeying the Shan-Chen equation of state [44]. In order to assess the static behavior, we take a two-dimensional periodic mesh made of 320 x 320 nodes, and prepare the system by creating a circular drop of density $\rho = 2.0$ and radius $R = 40$ in lattice units, immersed in the second background phase at lower density $\rho_b = 0.16$. Further, the strength of non-ideal interactions was set equal to $G = -5$, $G/G_{crit}^o = 1.25$ where $G_{crit}^o = -4$ is the critical Shan-Chen coupling at the critical density $\rho_{crit} = \ln 2$ in the absence of electric fields. Since we aim to model a leaky dielectric fluid, the ratio Q_s/Q_b is taken equal to 10, so that the largest part of the charge lies over the surface. The total charge $Q = Q_s + Q_b$ was set equal to 2.13, and $q(\vec{r})$ computed by Eq. 14. Whenever the Poisson equation is solved, a uniform negative charge is added to obtain a system with net charge zero. Hence, the electric force $\vec{F}_{el} = q(-\nabla\phi)$ is added into the LB scheme by Eq. 6, where q is computed by Eq. 14 with K_d equal to 1. The liquid is Newtonian with kinematic viscosity $\nu = 1/6$.

The stationary configuration of the described system is obtained after 1000 time steps. Hence, we inspect the electric field (see Fig. 1) at rest conditions in order to analyze the balance of forces acting at the interface, including Shan-Chen pressure and capillary and electrostatic forces, the latter pointing normal to the interface (see panel b of Fig. 1). Here, we observe that the largest part of the electric field is located over the liquid surface where the charge distribution is higher. In particular, at the boundary of the drop the magnitude of the electric field $|\vec{E}|$ is equal to $3.5 \cdot 10^{-3}$.

It is of interest to estimate the various forces which concur to provide a stable configuration of the droplet. The mechanical balance reads as follows:

$$p_L + p_{el} = p_V + p_{cap} \tag{20}$$

where p_L and p_V are the liquid and vapour pressure, respectively, $p_{cap} = \sigma/R$ is the capillary pressure (given the surface tension σ and the drop radius R), and p_{el} is the repulsive electrostatic pressure. The latter can be estimated by standard considerations in electrostatics,

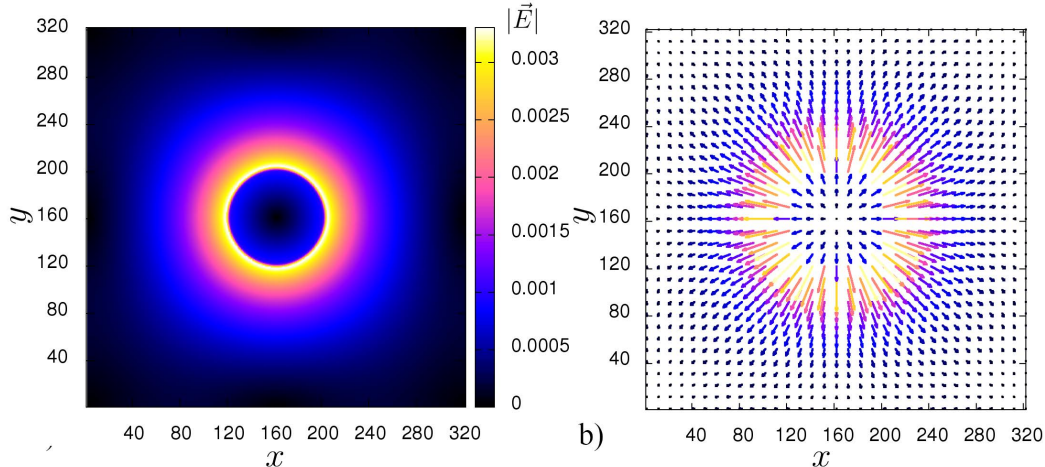


Figure 1. Profile of the electric field magnitude $|\vec{E}|$ in (panel a), and its vectorial representation (panel b). Both quantities refer to the charged drop at rest.

namely:

$$p_{el} = \frac{Q_s \vec{E}_s \cdot \vec{n}}{2\pi R} \quad (21)$$

where E_s is the electric field at the surface.

$$\frac{p_{el}}{p_{cap}} = \frac{Q_s E_s}{2\pi\sigma} \quad (22)$$

In actual numbers with $\sigma = 5.8 \cdot 10^{-2}$, this ratio is equal to 1/50. This shows that electrostatic forces act as a small perturbation on top of the neutral multiphase physics.

Next, we investigate the effects of a uniform external electric field E_{ext} of magnitude pointing along the x axis. Using the previous configuration at the equilibrium as starting point of our simulation, we set E_{ext} at two different values equal to 0.1 and 0.5. For each one of the two cases, we report a snapshot of the fluid density ρ taken as soon as the liquid drop touches the point of coordinates (280,160) in lattice units. The set in Fig. 2 highlights the significant motion of the charged drop towards right in accordance with the direction of the electric field. In the figure, we note that a sizable change in the drop shape is present only for the case $E_{ext} = 0.5$. In order to elucidate this effect, it is instructive to assess the strength of the electrostatic field in units of capillary forces, namely:

$$\tilde{E} \equiv \frac{QE_{ext}}{2\pi R} \frac{R}{\sigma} = \frac{QE_{ext}}{2\pi\sigma} \quad (23)$$

In actual numbers, this ratio is equal to 0.5 and 3 for the case at lower and higher E_{ext} , respectively. This shows that the electric force magnitude is sufficiently large to provide an

alteration of its shape only in the case at higher E_{ext} . In particular, the shape shows an elongation towards the direction of the electric field E_{ext} , which results from the effect of the curvature on the surface charge.

In Fig. 3, we report the alteration of charge density due to the mean curvature term K of Eq. 14. The alteration is estimated as $\delta_q = q - q_{K=0}$, where $q_{K=0}$ is computed with Eq. 14 with $K = 0$ everywhere, corresponding to a constant surface charge model without curvature effect correction. Here, we note an accumulation of charge on the rightmost part of the drop, where the mean curvature K shows a maximum value equal to $5.17 \cdot 10^{-2}$, which corresponds to a charge accumulation δ_q equal to $1 \cdot 10^{-3}$, in the following denoted δ_q^+ . The accumulation of charge is counterbalanced by a negative charge δ_q^- distributed over the almost straight surface part of the drop (just behind the rightmost protrusion in Fig. 3). Both partial charges δ_q^+ and δ_q^- favor the presence of a protrusion in the drop shape. In order to analyze this effect, we report in Fig. 4 the mean curvature computed at the same time $t = 1250\delta t$ for two simulations, both at $E_{ext} = 0.5$ differing for the inclusion of the curvature effects in the constant surface charge model of Eq. 14. Even though the circular shape of the drop is deformed by the external electric field in both cases, the curvature effects increases the protrusion on the drop shape (see Fig. 4 panel b). Further, the charge differences provide a shift in the electric force acting on the drop surface, the effect of which accumulates in time, so that the alteration in the drop shape increases in time.

B. Charged multiphase jet in electrospinning setup

We set up a system modeling the electrospinning process, containing a charged Shan-Chen fluid. The system is a mesh made of 320×320 nodes (see Fig. 5). The system geometry presents, on the left side, a nozzle of diameter $D = 40$ that reproduces the needle of the actual electrospinning apparatus where the charged fluid is injected, while on the up and bottom sides we impose the bounce back boundary condition. As a consequence, the system is open with the inlet nodes located inside (left side) the nozzle (at $x = 1$). Similarly, we set outlet nodes on the right side (at $x = 320$) where the jet will impinge under the effect of the external electric field. Such electric field is chosen to mimic the potential difference that is normally applied between the nozzle and a conductive collector in the real electrospinning setup [51]. The computational setup is quite sensitive to the choice of

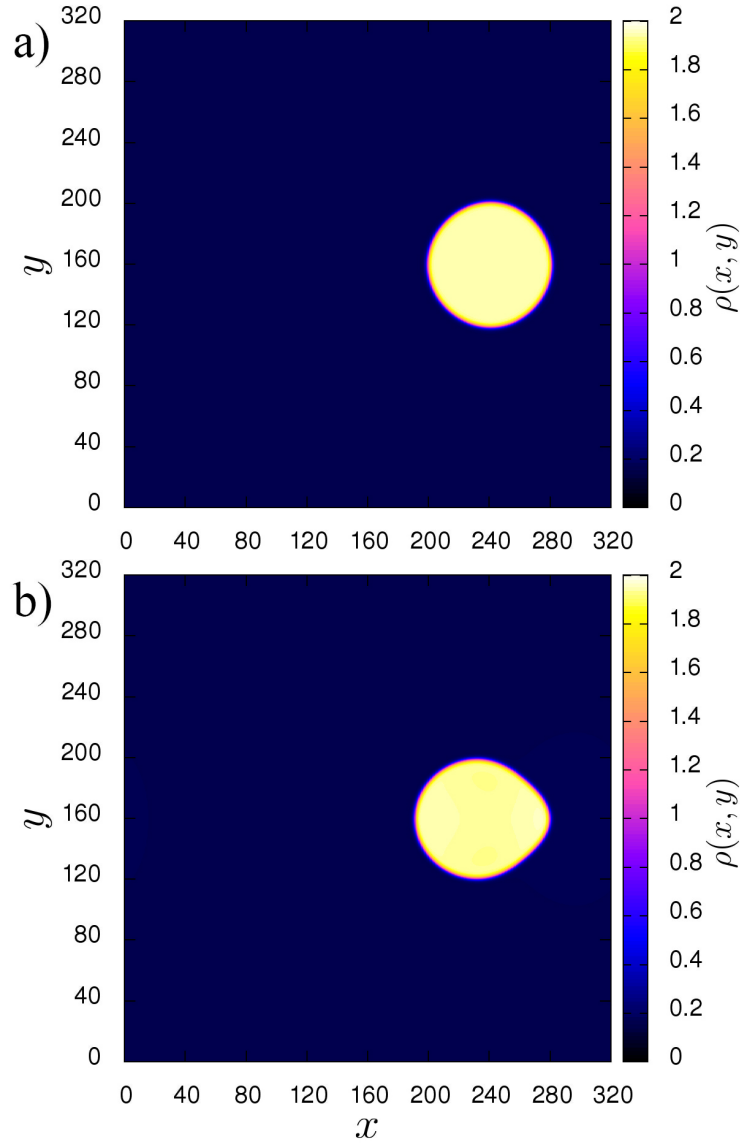


Figure 2. Two snapshots of density ρ for a charged drop under an external electric field E_{ext} equal to 0.1 (panel a) and 0.5 (panel b) taken as soon as the drop reaches the point of coordinates (280, 160).

the simulation parameters, and numerical stability has to be guaranteed by finely tuning several parameters, in particular: the density and velocity of inlet and outlet nodes, the Shan-Chen coupling constants of fluid-fluid and fluid-wall interactions, the charge constant and the magnitude of the external electric field. After preliminary simulations, we obtain a consistent set of parameters that guarantees a stable and well-shaped charged jet ejected from the nozzle.

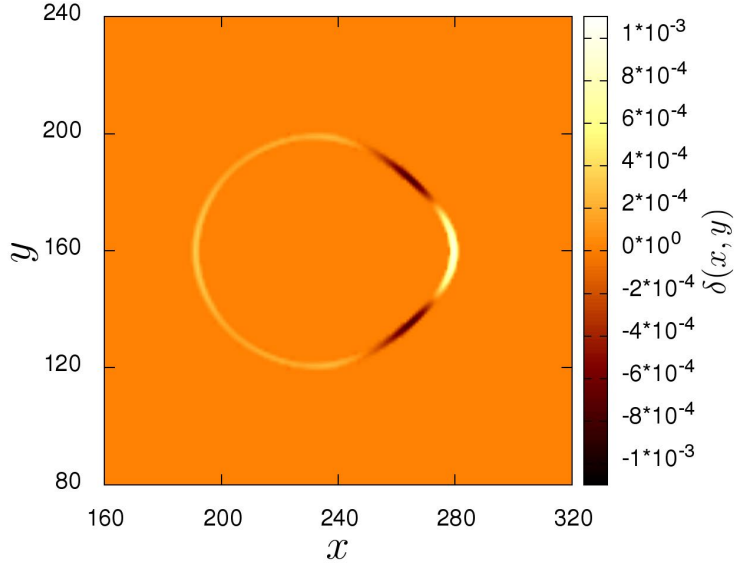


Figure 3. Alteration of charge density q due to the mean curvature K . The alteration is estimated as $\delta_q = q - q_{K=0}$, where $q_{K=0}$ is computed with Eq. 14 with $K = 0$ everywhere.

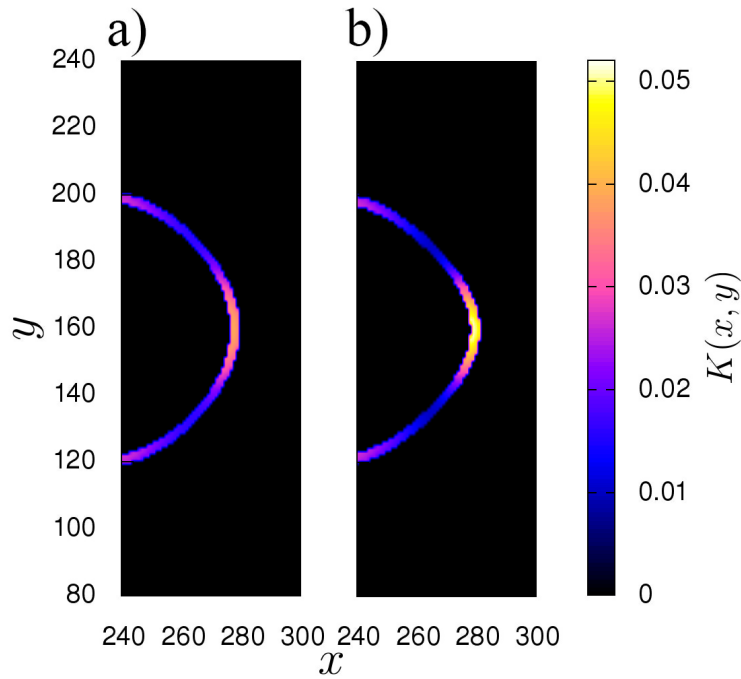


Figure 4. Mean curvature $K(x, y,)$ computed at the same time $t = 1250 \delta t$ with same surface charge Q_s at $E_{ext} = 0.5$ with two constant surface charge models: without the curvature effect (panel a), and with the curvature effect (panel b).

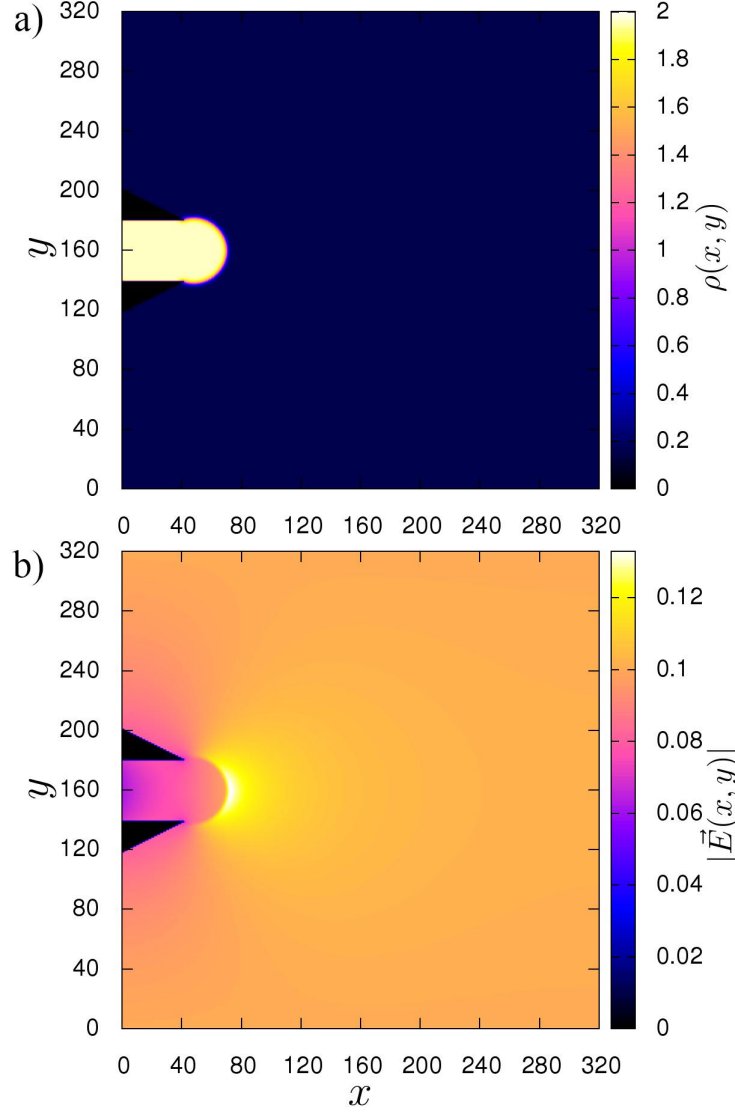


Figure 5. In panel a, the density distribution ρ of the initial configuration for the electrospinning setup. In panel b, the electric field magnitude $|\vec{E}|$.

The initial density of the two phases are 2.0 and 0.16 for the liquid and gaseous phase, respectively. The initial configuration consists of the liquid phase filling the inner space of nozzle with a liquid drop just outside the needle (see Fig. 5 panel a). All remaining fluid nodes are initialized to gaseous density.

Both the Shan-Chen constants for the fluid-fluid G and fluid-wall G_w interaction are set to -5 . As in previous section, for the resolution of the Poisson equation a uniform negative charge is added to the system in order to counterbalance the positive charge and obtain a system with net charge zero. Further, we impose Dirichlet boundary condition in the

following form: we impose the electric potential $\phi_l = 0$ on the left side ($x = 0$), while the electric potential on the right side ($x = 321$) was set equal to $\phi_r = -32.2$, providing a background electric field $E_{back} = (\phi_r - \phi_l)/322$, which is imposed between the two opposite sides (left-right) of the system. On the upper and bottom sides, the Dirichlet boundary conditions are set equal to the $\phi_u(x) = \phi_b(x) = x(\phi_r - \phi_l)/322$. Note that the last condition is equivalent to impose an electric field \vec{E} of magnitude 0.1 oriented along the x-axis.

Since in a typical electrospinning setup the liquid phase is always connected to a generator addressing a charge, it is reasonable to assume that, whenever the stretching of the liquid jet increases the jet interface, extra charge rapidly reaches the liquid boundary in order to preserve the value of charge surface density. As a consequence, the charge conservation condition can not be applied (the liquid jet is not isolated). Instead, we assume the conservation condition of the surface charge density value for the same mean curvature, so that Eq. 14 is rewritten as

$$q(\vec{r}) = \xi_b \rho(\vec{r}) \theta(\rho(\vec{r}); \rho_0) + \xi_s |\nabla \rho(\vec{r})|^2 [1 + (K/K_d)^{\frac{1}{4}}], \quad (24)$$

where we have adopted a similar condition also for the bulk charge term, being ξ_b and ξ_s two proportionality constants, in the following taken equal to $1 \cdot 10^{-4}$ and $6 \cdot 10^{-2}$, respectively. Note that the two proportionality constants were tuned in order to obtain a mean ratio Q_s/Q_b between the surface and bulk charge close to the target value 10, as in the previous case.

At the inlet we set the fluid velocity in accordance with the Poiseuille velocity profile, while the density is set to 2.0. In particular, at each time step we compute the mean velocity of the fluid inside the nozzle, then we used this value to set up the Poiseuille profile. As a consequence, the velocities at the inlet nodes are not fixed but can change during the simulation according to the actual mean velocity measured inside the nozzle. The outlet nodes (on the right edge) are put in contact with a gas reservoir with $\rho = 0.16$, so that the liquid exits by diffusion/advection.

We run three different simulations, all starting from the same initial configuration. In the first simulation the liquid is Newtonian with kinematic viscosity $\nu = 1/6$, in the following denoted *case 1*. In the other two, we employ the Carreau model (see Subsec. II A) with zero shear kinematic viscosity $\nu_0 = 1/6$, and infinite viscosity $\nu_\infty = 0.001$. The flow index n is taken equal to 0.75, and 0.5, for the case labeled *b*, and *c*, respectively, while the retardation time λ was set equal to 1000 for all the two last cases.

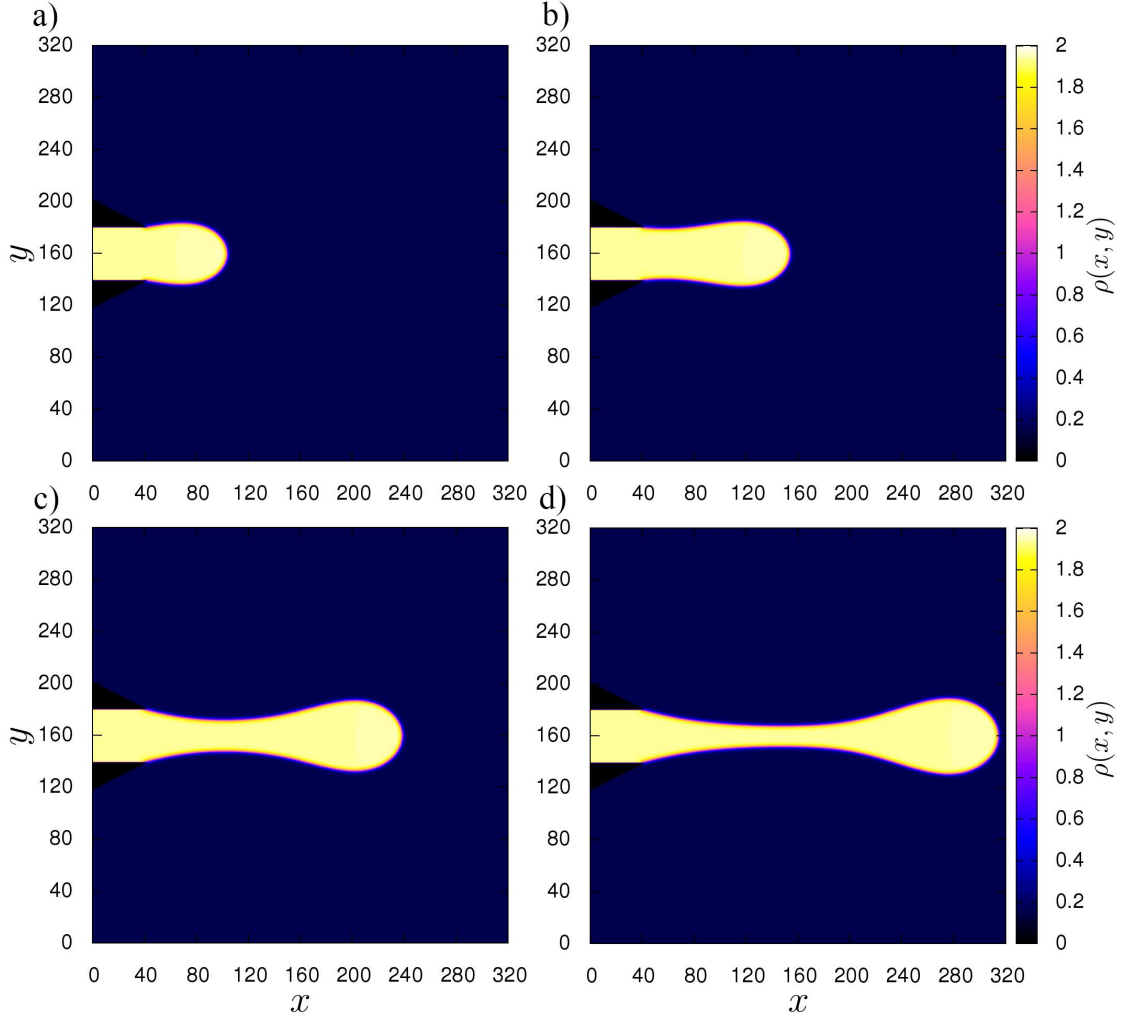


Figure 6. Series of snapshots of the fluid density ρ for the electrospinning simulation *case b* with index flow $n = 0.75$ and retardation time $\lambda = 1000$ taken at timesteps 2500(a), 5000(b), 7500(d), and 8800(d).

The internal electric field computed by the Poisson solver (see Section 2) is computed on-the-fly during the simulation. In panel b of Fig. 5 we report the electric field magnitude $|\vec{E}|$ for the initial configuration. Here, we note a maximum value in $|\vec{E}|$ close to the drop interface, which is due to the higher surface charge density. Further, a lower value of $|\vec{E}|$ is observed in the nozzle as a consequence of the larger dielectric constant $\varepsilon \simeq 3$ in the liquid phase (versus $\varepsilon \simeq 1$ in the gaseous phase).

We now report in Fig. 6 several snapshots taken over the time evolution of the system labeled *case b*. In all the cases, we observe the formation of a liquid charged jet, which is

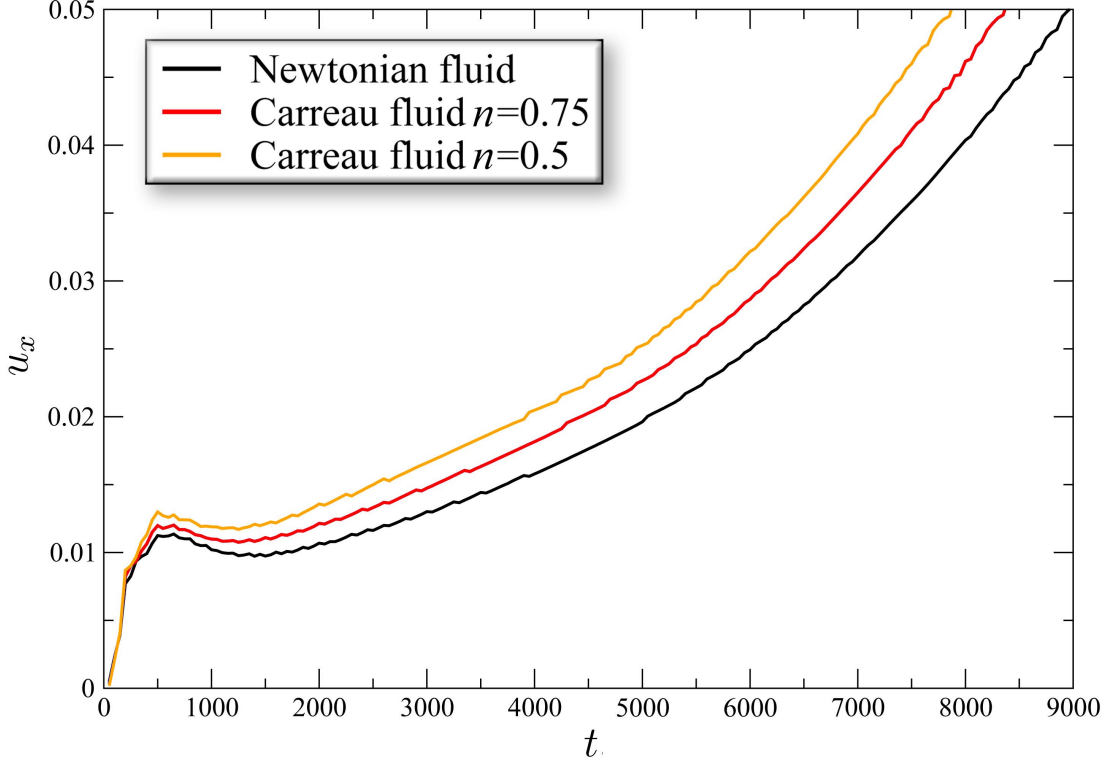


Figure 7. Velocity component u_x registered at the extreme point (rightest point) of the drop surface versus time for all the three cases under investigation.

ejected from the nozzle. Further, we report in Fig. 7 the velocity component u_x measured at the extreme point (rightest point) of the drop surface versus time t . Here, for all cases under investigation we note that the velocity trend show the presence of a quasi-stationary point, where the viscous forces balances the external electric force in agreement with previous theoretical investigations [10, 52]. After the jet touches the collector, the jet shape fluctuates around a mean profile, providing a stationary regime. In particular, at this stage the jet shows an hyperbolic profile (see Fig. 8 panel b) which appears to be in qualitative agreement with the characteristic shape of the jet experimentally observed close to the injecting nozzle by the Rafailovich and Zussman groups [53] (see Fig. 8 panel a) and in consistency with previous theoretical results on the jet conical shape [11, 54–58].

In order to characterize the stationary regime, we report in panel c of Fig. 8 the magnitude of the velocity field, and the line integral convolution (LIC) visualization technique [59], highlighting the fine details of the flow field. As expected, we observe a higher value of $u(x, z)$ along the jet towards the collector. In particular, we analyze the profile of the

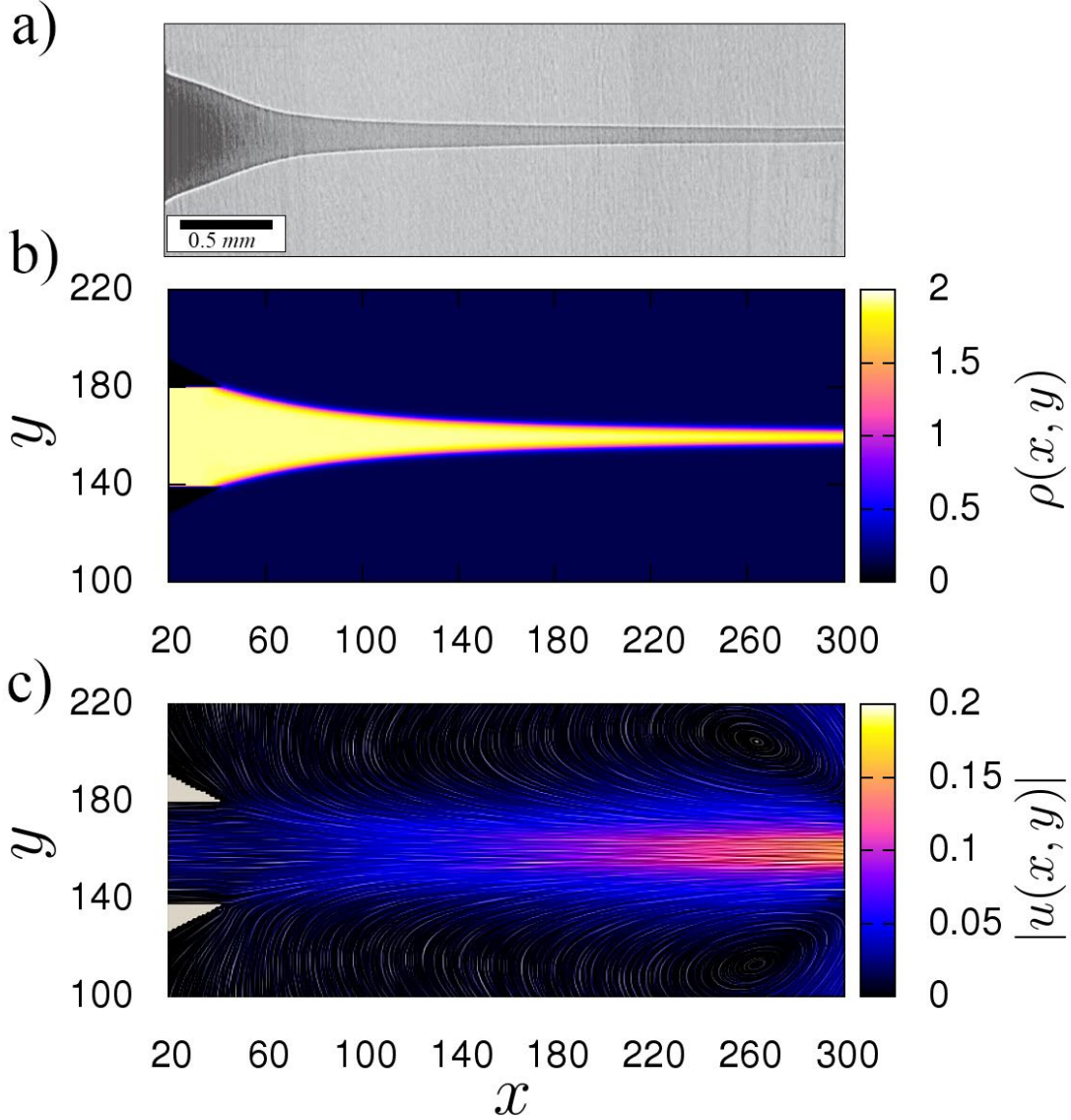


Figure 8. In panel (a), a rectilinear section of a jet in an electrospinning experiment of a solution of 5 wt% polyethylene oxide in water. Figure adapted with permission from Ref. [53]. Copyrighted by the American Physical Society. In panel (b), a snapshot of the fluid density ρ in the stationary regime after the jet has touched the right side of the simulation box in the *case b*. In panel (c), the corresponding velocity field magnitude $|u(x, y)|$ and the LIC representation of the velocity field.

velocity in a jet cross section along what is generally observed in the experimental process.

We investigate the effect of pseudoplastic rheology on the stress tensor $\mathbf{\Pi}$. In panel a of Fig. 9 we report the mean value of the stress $\mathbf{\Pi}$ measured along the central axis of the jet $y = 160$, and averaged over a time interval of 15000 steps in the stationary regime for

the three cases under investigation. Here, we note a decreasing trend of the the stress by increasing the pseudoplasticity of the fluid (decreasing the flow index n). Nonetheless, we observe a small shift in the stress magnitude. This is essentially due to the low value of retardation time λ in the Carreau model adopted in our simulation, which provides a small decrease in the kinematic viscosity ν . In order to clarify the this point, we report in panel b of Fig. 9 the mean value of the kinematic viscosity $\langle \nu \rangle$ again assessed along the central axis of the jet $y = 160$, and averaged over the stationary regime time, where we observe a small decrease of $\langle \nu \rangle$ along the stretching direction as a function of the pseudoplastic behavior in the fluid. These results look promising, and we plan to investigate systematically the effect of the rheological parameters on the jet dynamics in a future work.

IV. SUMMARY

Summarizing, we developed a Shan-Chen model for charged leaky dielectric fluids mainly aimed at modeling the electrospinning process. The curvature effects on the charge surface were included in our theoretical treatment, and we generalized the model to non-Newtonian flows in order to account for the peculiar rheological behavior. Different scenarios were investigated to test the model. We initially investigated the effect of strong electric fields on the droplet shape evolution. We also probed the jet formation under electrospinning-like conditions, obtaining a good agreement with both experimental results and previous theoretical works present in literature. At first glance, the pseudoplastic behavior alters the jet dynamics, although a more systematic investigation requires an extensive test of the rheological parameters. Work along these lines is currently underway.

The preliminary applications of the presented LB model look promising, although more systematic numerical investigations, as well as theoretical analysis need to be undertaken. Nonetheless, the actual effort can be regarded as a significant forward step to extend the applicability of the LB method to the context of electrospinning systems, providing a useful computational tool in completion of the others presently available in literature.

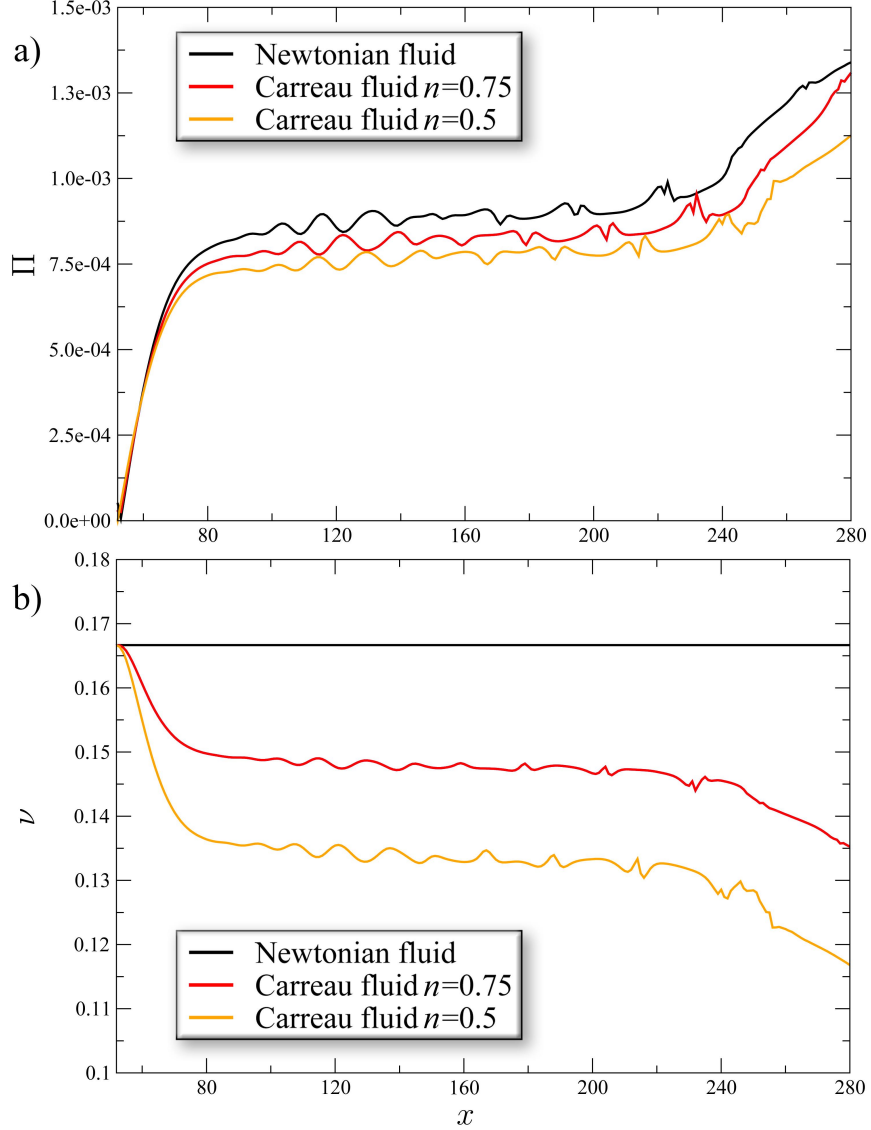


Figure 9. In panel (a), the mean value of the stress $\mathbf{\Pi}$ computed as matrix 2-norm $\langle \|\mathbf{\Pi}\|_2 \rangle_t$ of the stress tensor measured along the central axis of the jet $y = 160$ averaged over a time interval of 15000 steps. In panel (b), the mean value of the kinematic viscosity ν computed with Eq. 19 along the central axis of the jet $y = 160$, and averaged over a time interval of 15000 steps.

ACKNOWLEDGMENTS

The research leading to these results has received funding from the European Research Council under the European Union’s Seventh Framework Programme (FP/2007-2013)/ERC Grant Agreement n. 306357 ("NANO-JETS"), and under the European Union’s Horizon 2020 Framework Programme (No. FP/2014- 2020)/ERC Grant Agreement No. 739964

("COPMAT").

Appendix: Units Conversion Table

| Symbol | Definition | 2-d lattice units | 3-d cgs units |
|----------------|-----------------------|--|---|
| ρ | Mass density | $1 \Delta m \Delta l^{-2}$ | 0.5 g cm^{-3} |
| u | Velocity | $1 \Delta l \Delta t^{-1}$ | 1200 cm s^{-1} |
| ν | Kinematic viscosity | $1 \Delta l^2 \Delta t^{-1}$ | $1.2 \text{ cm}^2 \text{ s}^{-1}$ |
| q | Charge | $1 \Delta l^{3/2} \Delta m^{1/2} \Delta t^{-1}$ | $8.5 \cdot 10^{-4} \text{ statC}$ |
| E | Electric field | $1 \Delta l^{-1/2} \Delta m^{1/2} \Delta t^{-1}$ | $848.5 \text{ statV cm}^{-1}$ |
| ϕ | Electric potential | $1 \Delta l^{1/2} \Delta m^{1/2} \Delta t^{-1}$ | $8.485 \cdot 10^{-1} \text{ statV}$ |
| ε | Relative permittivity | — | — |
| K | Mean curvature | $1 \Delta l^{-1}$ | 1000 cm^{-1} |
| $\dot{\gamma}$ | Shear rate | $1 \Delta t^{-1}$ | $1.2 \cdot 10^6 \text{ s}^{-1}$ |
| Π | Stress | $1 \Delta m \Delta t^{-2}$ | $7.2 \cdot 10^5 \text{ g cm}^{-1} \text{ s}^{-2}$ |
| λ | Retardation time | $1 \Delta t$ | $8.3 \cdot 10^{-7} \text{ s}$ |
| n | Index flow | — | — |
| p | Pressure | $1 \Delta m \Delta t^{-2}$ | $7.2 \cdot 10^5 \text{ g cm}^{-1} \text{ s}^{-2}$ |
| σ | Surface tension | $1 \Delta l \Delta m \Delta t^{-2}$ | 720 g s^{-2} |

Table I. Symbols employed in order of appearance, their definitions, relative dimensions in 2-d lattice units, and conversion values in 3-d Gaussian centimetre-gram-second (cgs) system of units. The conversion to 3-d dimension units is obtained by multiplying the 2-d square area Δl^2 for an extra node Δl along the z-axis. Note that Δm denotes the mass unit equal to $5 \cdot 10^{-10} \text{ g}$ (water density), Δl the length unit equal to 10^{-3} cm , and time step Δt is the time unit equal to $8.3 \cdot 10^{-7} \text{ s}$. The last number was tuned in order to set the kinematic viscosity $\nu = 1/6 \Delta l^2 \Delta t^{-1} = 0.2 \text{ cm}^2 \text{ s}^{-1}$ in similarity with the viscosity value adopted in the Lagrangian model of Ref. [12].

-
- [1] A. L. Yarin, B. Pourdeyhimi, and S. Ramakrishna, *Fundamentals and applications of micro- and nanofibers* (Cambridge University Press, 2014).
- [2] J. H. Wendorff, S. Agarwal, and A. Greiner, *Electrospinning: materials, processing, and applications* (John Wiley & Sons, 2012).
- [3] D. Pisignano, *Polymer Nanofibers: Building Blocks for Nanotechnology*, Vol. 29 (Royal Society of Chemistry, 2013).
- [4] A. Frenot and I. S. Chronakis, *Current opinion in colloid & interface science* **8**, 64 (2003).
- [5] Z.-M. Huang, Y.-Z. Zhang, M. Kotaki, and S. Ramakrishna, *Composites science and technology* **63**, 2223 (2003).
- [6] D. Li, Y. Wang, and Y. Xia, *Advanced Materials* **16**, 361 (2004).
- [7] A. Greiner and J. H. Wendorff, *Angewandte Chemie International Edition* **46**, 5670 (2007).
- [8] C. P. Carroll, E. Zhmayev, V. Kalra, Y. L. Joo, *et al.*, *Korea-Australia Rheology Journal* **20**, 153 (2008).
- [9] L. Persano, A. Camposeo, C. Tekmen, and D. Pisignano, *Macromolecular Materials and Engineering* **298**, 504 (2013).
- [10] D. H. Reneker, A. L. Yarin, H. Fong, and S. Koombhongse, *Journal of Applied physics* **87**, 4531 (2000).
- [11] J. Feng, *Journal of Non-Newtonian Fluid Mechanics* **116**, 55 (2003).
- [12] M. Lauricella, G. Pontrelli, I. Coluzza, D. Pisignano, and S. Succi, *Computer Physics Communications* **197**, 227 (2015).
- [13] M. Lauricella, G. Pontrelli, D. Pisignano, and S. Succi, *Journal of Computational Science* **17**, 325 (2016).
- [14] M. Lauricella, D. Pisignano, and S. Succi, *The journal of physical chemistry. A* **120**, 4884 (2016).
- [15] A. M. Ganan-Calvo, *Journal of Fluid Mechanics* **335**, 165 (1997).
- [16] M. M. Hohman, M. Shin, G. Rutledge, and M. P. Brenner, *Physics of fluids* **13**, 2201 (2001).
- [17] A. L. Yarin, S. Koombhongse, and D. H. Reneker, *Journal of applied physics* **89**, 3018 (2001).
- [18] B. Li and D. Y. Kwok, *Physical review letters* **90**, 124502 (2003).
- [19] A. Kupershtokh and D. Medvedev, *Journal of electrostatics* **64**, 581 (2006).

- [20] W. Huang, Y. Li, and Q. Liu, Chinese Science Bulletin **52**, 3319 (2007).
- [21] S. Gong, P. Cheng, and X. Quan, International Journal of Heat and Mass Transfer **53**, 5863 (2010).
- [22] D. Medvedev, Procedia Computer Science **1**, 811 (2010).
- [23] H. Bararnia and D. Ganji, Advanced Powder Technology **24**, 992 (2013).
- [24] A. L. Kupershtokh, Computers & Mathematics with Applications **67**, 340 (2014).
- [25] L. D. Landau, J. Bell, M. Kearsley, L. Pitaevskii, E. Lifshitz, and J. Sykes, *Electrodynamics of continuous media*, Vol. 8 (elsevier, 2013).
- [26] G. Taylor, *Proceedings of the Royal Society of London A: Mathematical, Physical and Engineering Sciences*, **280**, 383 (1964).
- [27] G. Taylor, *Proceedings of the Royal Society of London A: Mathematical, Physical and Engineering Sciences*, **291**, 159 (1966).
- [28] G. Taylor, *Proceedings of the Royal Society of London A: Mathematical, Physical and Engineering Sciences*, **313**, 453 (1969).
- [29] D. Saville, Annual review of fluid mechanics **29**, 27 (1997).
- [30] J. Hua, L. K. Lim, and C.-H. Wang, Physics of Fluids **20**, 113302 (2008).
- [31] Z.-T. Li, G.-J. Li, H.-B. Huang, and X.-Y. Lu, International Journal of Modern Physics C **22**, 729 (2011).
- [32] S. Chikatamarla, S. Ansumali, and I. Karlin, Physical review letters **97**, 010201 (2006).
- [33] S. Ansumali and I. V. Karlin, Physical Review E **65**, 056312 (2002).
- [34] B. Dorschner, F. Bösch, S. S. Chikatamarla, K. Boulouchos, and I. V. Karlin, Journal of Fluid Mechanics **801**, 623 (2016).
- [35] I. Karlin, A. Ferrante, and H. C. Öttinger, EPL (Europhysics Letters) **47**, 182 (1999).
- [36] S. Ansumali, I. V. Karlin, and H. C. Öttinger, EPL (Europhysics Letters) **63**, 798 (2003).
- [37] A. Kupershtokh, D. Medvedev, and D. Karpov, Computers & Mathematics with Applications **58**, 965 (2009).
- [38] A. Quarteroni and A. Valli, *Numerical approximation of partial differential equations*, Vol. 23 (Springer Science & Business Media, 2008).
- [39] A. M. Gañán-Calvo, Journal of fluid mechanics **507**, 203 (2004).
- [40] I. McAllister, Journal of Physics D: Applied Physics **23**, 359 (1990).
- [41] T. Spencer, I. Halliday, and C. Care, Physical Review E **82**, 066701 (2010).

- [42] A. L. Yarin, S. Koombhongse, and D. H. Reneker, *Journal of applied physics* **90**, 4836 (2001).
- [43] H. Huang, M. Sukop, and X. Lu, *Multiphase lattice Boltzmann methods: Theory and application* (John Wiley & Sons, 2015).
- [44] X. Shan and H. Chen, *Physical Review E* **47**, 1815 (1993).
- [45] G. Pontrelli, S. Ubertini, and S. Succi, *Journal of Statistical Mechanics: Theory and Experiment* **2009**, P06005 (2009).
- [46] S. Gabbanelli, G. Drazer, and J. Koplik, *Physical review E* **72**, 046312 (2005).
- [47] E. Aharonov and D. H. Rothman, *Geophysical Research Letters* **20**, 679 (1993).
- [48] R. Ouared and B. Chopard, *Journal of statistical physics* **121**, 209 (2005).
- [49] S. Agarwal, M. Burgard, A. Greiner, and J. Wendorff, *Electrospinning: A Practical Guide to Nanofibers* (Walter de Gruyter GmbH & Co KG, 2016).
- [50] R. W. Johnson, *Handbook of fluid dynamics* (Crc Press, 2016).
- [51] M. Montinaro, V. Fasano, M. Moffa, A. Camposeo, L. Persano, M. Lauricella, S. Succi, and D. Pisignano, *Soft matter* **11**, 3424 (2015).
- [52] M. Lauricella, G. Pontrelli, D. Pisignano, and S. Succi, *Molecular Physics* **113**, 2435 (2015).
- [53] I. Greenfeld, A. Arinstein, K. Fezzaa, M. H. Rafailovich, and E. Zussman, *Physical Review E* **84**, 041806 (2011).
- [54] S. Reznik and E. Zussman, *Physical Review E* **81**, 026313 (2010).
- [55] F. Higuera, *Journal of Fluid Mechanics* **484**, 303 (2003).
- [56] M. M. Hohman, M. Shin, G. Rutledge, and M. P. Brenner, *Physics of fluids* **13**, 2221 (2001).
- [57] R. P. A. Hartman, D. Brunner, D. Camelot, J. Marijnissen, and B. Scarlett, *Journal of Aerosol science* **30**, 823 (1999).
- [58] L. T. Cherney, *Journal of Fluid Mechanics* **378**, 167 (1999).
- [59] B. Cabral and L. C. Leedom, in *Proceedings of the 20th annual conference on Computer graphics and interactive techniques* (ACM, 1993) pp. 263–270.